Order improvement of surface nanopatterns via substrate rocking under ion bombardment: Experiments and nonlinear models

Sujin Jo,[1] Jihee Jun,[1] Eunsu Lee,[1] S. M. Yoon [ORCID],[2] J. Seo,[3] J. Muñoz-García [ORCID],[4] R. Cuerno [ORCID],[4] and J.-S. Kim [ORCID][1,3,*]

[1]*Department of Physics, Sook-Myung Women's University, Seoul 04310, Korea*

[2]*Materials and Life Science Research Division, Korea Institute of Science and Technology, Seoul 02792, Korea*

[3]*Institute of Advanced Materials and Systems, Sook-Myung Women's University, Seoul 04310, Korea*

[4]*Departamento de Matemáticas and Grupo Interdisciplinar de Sistemas Complejos (GISC),*
Universidad Carlos III de Madrid, 28911 Leganés, Spain

Surface nanopatterns formed by ion beam sputtering (IBS) frequently include a high density of structural defects, which seriously limit their practical applications. Recent theoretical work [M. P. Harrison and R. M. Bradley, Phys. Rev. E **93**, 040802(R) (2016)], based on the anisotropic Kuramoto-Sivashinsky (aKS) equation, proposes that rocking a substrate during IBS can produce defect-free patterns under certain requirements. We find experimentally, via low-energy Kr^+ irradiation of Si and amorphous carbon targets, that rocking the substrates generally improves the order of the ripple patterns. Indeed, order is improved even when conditions required in the aKS model may not be satisfied. Through numerical simulations, we show that a suitable generalization of this equation, in which conserved nonlinear effects are incorporated, reproduces satisfactorily the pattern order in our experimental conditions.

I. INTRODUCTION

Ion beam sputtering (IBS) is a facile tool to fabricate nanopatterns at surfaces via physical self-assembly induced by bombardment of solid targets with energetic ions [1–4]. For near-normal incidence of the ion beam, nanodot patterns form [5,6], while nanoripple patterns emerge under oblique incidence angle conditions [7,8]. By changing the beam energy E_{ion}, ion flux f, total ion fluence F (which is the product of f times the total irradiation time), and the ion source, as well as the ion incidence angle, the scales of the patterns can be controlled. Moreover, IBS is fast, cheap, and easy to control; it can be easily scaled to the sizes requested for various applications and is applicable to any solid substrates, all of which makes IBS an attractive tool for nanopatterning.

IBS-produced patterns, however, include significant densities of structural defects, a common drawback of this self-assembly process which often limits its applications [4], there having been experimental proposals to decrease the number of such defects, e.g. by sequential IBS [9]. Recently, Harrison and Bradley (HB) [10] predicted IBS of periodically rocked substrates to produce virtually defect-free patterns. They consider the anisotropic Kuramoto-Sivashinsky (aKS) equation [1,11,12] as a long used nonlinear model for the evolution of the surface height $h(x, y, t)$ in IBS [13], namely,

$$h_t = -Ah_{xx} + A'h_{yy} - B\nabla^4 h + \frac{1}{2}(\lambda h_x^2 + \lambda' h_y^2), \quad (1)$$

where t is time, x (y) is the target plane coordinate along (perpendicular to) the projection of the ion beam direction, and subscripts denote partial derivatives; the coefficients A

and A' model curvature-dependent erosion [14], B quantifies the relevance of thermal surface diffusion according to the seminal proposal in Ref. [14], and λ, λ' are coefficients of the so-called Kardar-Parisi-Zhang (KPZ) nonlinearities [15], which reflect the dependence of the erosion rate on the local slopes [1,11]. While coefficient B in Eq. (1) is beam independent [14], A, A', λ, and λ' do depend on irradiation conditions, specifically on the angle of incidence θ between the ion beam and the normal to the unrocked target [1,11]. Thus, periodically rocking the substrate (changing θ between two fixed values α and β, see Fig. 1) makes these coefficients change periodically in time.

For $A, A' > 0$, Eq. (1) predicts a ripple structure which is periodic along the x direction, with ripple ridges along the y direction. The discussion of the effect of rocking becomes simplified for the case in which h is independent of y, Eq. (1) describing a one-dimensional (1D) substrate [10]. Allowing the polar angle θ to change periodically between two values α and β, as shown in Fig. 1, the numerical study of Eq. (1) predicts nearly defect-free ripple patterns to form on the rocked surface under certain rocking and sputter conditions, while the unrocked surface shows a significant density of structural defects under otherwise the same sputter conditions [10].

The *first* condition for defect-free pattern formation is that λ should change signs during rocking [10]. Intuitively, this is because, in absence of nonlinear terms, the linear instability that occurs in Eq. (1) amplifies a specific Fourier mode of the height exponentially faster than all other modes, which improves surface ordering. Meanwhile, the λ-nonlinearity arrests amplitude growth once it sets in with a nonzero coefficient [16,17]. Based on theoretical and experimental indications [1,18], it is expected that $\lambda(\theta_c) = 0$ for a certain value of the

*jskim@sookmyung.ac.kr
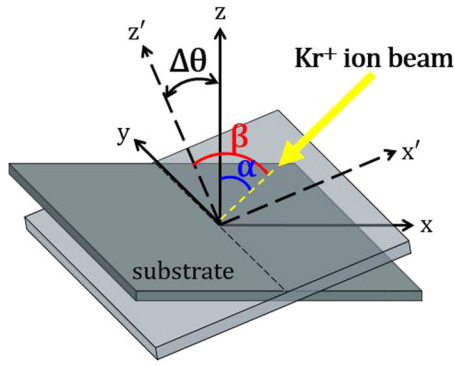
FIG. 1. Schematic of the rocking geometry during IBS, where θ is the polar incidence angle between the Kr^+ beam (yellow arrow) and the (unrocked) surface normal (so that $\theta = \alpha$ in this sketch). The sample is rocked around the y axis, which is perpendicular to the projection of the beam on the (x, y) substrate plane, so θ changes periodically between the fixed values α and β, with $\Delta\theta = \beta - \alpha$ being the span of polar angles during rocking.

incidence angle θ_c. Thus, a practical suggestion for experiments made in Ref. [10] is to rock the substrate around the polar angle θ_L where the linear instability is maximized, assuming $\theta_L \approx \theta_c$. Hence, one should employ α and β values such that

$$\alpha < \theta_L < \beta. \tag{2}$$

Second, optimal order in the ripple pattern is numerically achieved [10] for rocking frequencies ν such that

$$0.2\sigma \lesssim \nu \lesssim 0.4\sigma, \tag{3}$$

where σ is the *linear* growth rate of the fastest growing mode on the unrocked substrate for the given sputter condition [14]. In the case of the aKS equation, Eq. (1), this linear growth rate is given by [10]

$$\sigma_{aKS} = \frac{A^2}{4B}, \tag{4}$$

so the midpoint value of the optimal frequency interval described by Eq. (3) is estimated by the aKS equation as

$$\nu_{aKS} \simeq \frac{0.3A^2}{4B}. \tag{5}$$

The analysis in Ref. [10] extends to 2D substrates and considers differences between stepwise (*discrete*) and sinusoidal (*continuous*) rocking, without substantial changes to the physical description just described.

In this paper, we test experimentally the theoretical predictions from Ref. [10] by rocking targets during IBS by a broad Kr^+ beam at low energies. To assess the generality of the behavior for different materials, we employ Si(100) and amorphous-carbon (a-C) targets. Our experiments show that substrate rocking during IBS indeed improves the order of the ensuing patterns compared with what is obtained on the unrocked surfaces for the same irradiation conditions. Within our experimental angular precision, the proposed rocking condition, Eq. (2), is not always required to obtain patterns with improved order. After checking numerically that Eq. (2) is indeed a requisite for defect-free patterns for the 2D aKS

equation, we search for a minimal extension of this model which can rationalize our experimental findings. We find that a suitable anisotropic generalization of the so-called extended KS (eKS) equation [6,16], which essentially adds a conserved-KPZ nonlinearity to Eq. (1), can elucidate qualitatively our morphological observations on the rocked surfaces within a unified theoretical description.

The paper is organized as follows. Our experimental methods are described in Sec. II. This is followed by Sec. III, which contains our experimental results for Si targets at two different energies, and for a-C targets at one of these energy values. This set of conditions allows us to assess the robustness of our results with respect to changes in the target composition and with respect to changes in the ion energy. The final part of this section is devoted to numerical results on the aKS and eKS equations, and to comparisons with the experimental results. Further discussion is provided in Sec. IV, which is followed by a summary and our conclusions in Sec. V.

II. EXPERIMENTAL

IBS is performed in a chamber with its base pressure in low 10^{-9} Torr. A broad Kr^+ beam is produced by a Kauffman-type ion source (Physical Electronics, 04-161 Sputter Ion Gun), with 10-mm diameter at the substrate when incident normal to the surface ($\theta = 0°$). The angular dispersion of the ion beam is approximately $\pm 1.35°$ as judged from the beam profile measurement provided by the manufacturer. The ion current is less than 10 μA at normal incidence, from which the incident ion flux f is estimated. Given that secondary electrons also contribute to the target current, the thus-determined value of f only sets an upper limit for the actual ion flux. The patterns formed on the substrates are imaged *ex situ* by an atomic force microscope (AFM; Park Systems XE-100) in the noncontact mode. The images are, then, analyzed using the SPIP (Image Metrology) package.

Concurrent with bombardment, both Si(100) and a-C substrates are rocked around an axis in the substrate plane, which we consider as the y axis, see Fig. 1, at a frequency ν in the 0.01 min^{-1} to 0.3 min^{-1} range. Substrate rocking is actuated by an ac-servo motor that is controlled by the LabView program [19]; the orientation of the sample is determined with a precision of $0.036°$. Continuous rocking produces much better ordered patterns than discrete rocking under otherwise identical sputter conditions, see Appendix A for details. Hence, we consider continuous rocking in the present paper.

III. RESULTS

A. Determination of optimal frequencies

To implement the scheme proposed by HB [10], we need to determine the optimal rocking frequencies described by Eq. (3). Experimentally, an estimate for the rate σ entering this condition can be obtained based on the behavior of the system at small irradiation times when the surface is assumed to be well described [2,4] by the linear approximation of, e.g., Eq. (1). The surface height is thus seen to evolve as a linear superposition of Fourier modes whose amplitudes grow or decay exponentially in time, being dominated by the one corresponding to the ripple structure [2,4]. This translates into
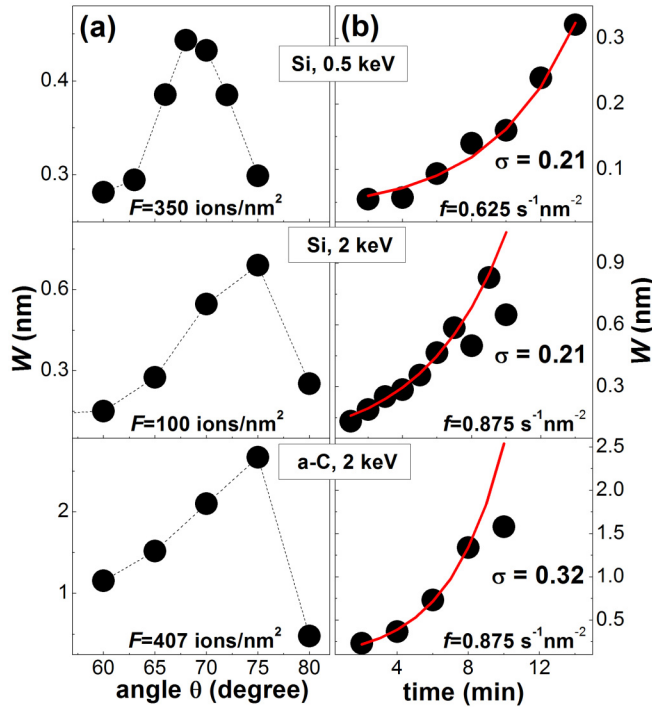
FIG. 2. (a) Surface width $W(\theta)$ as a function of the polar incidence angle θ for target atomic species, ion energy E_{ion}, and total ion fluence F as specified by the corresponding legend. The value of the incidence angle at which $W(\theta)$ reaches its maximum for the given sputter condition defines θ_L, see the text. The graphs have different vertical offsets for clarity of presentation and dashed lines are guides to the eye. (b) Evolution of $W(t)$ as a function of irradiation time t for experiments performed at the fixed $\theta = \theta_L$ value determined in the corresponding box of (a). The red solid lines show exponential fits to the observed behavior of the roughness in the early stage or linear regime as $W(t) \propto e^{\sigma t}$, where σ is assumed to be the linear growth rate of the fastest Fourier mode of the surface height, having min^{-1} units in all cases. The employed flux f is indicated at the bottom of each figure in the right column.

all height-related quantities. In particular, the surface width or roughness, W (root-mean-square of the height distribution), evolves in the linear regime as $W \propto e^{\sigma t}$, where the coefficient in the argument of the exponential factor is theoretically predicted [2,4] to be $\sigma = A_{max}^2/(4B)$, with A_{max} being the (absolute value of the) most negative among the coefficient of the second-order derivative terms, $A_{max} = A$ in Eq. (1). Note, in general, A is a θ-dependent quantity, while nonlinear effects compete with, and mitigate, the linear instability just described. In the context of the aKS equation, nonlinearities are expected to cancel exactly at some incidence angle $\theta = \theta_c$. HB then proposed [10] to experimentally measure the surface roughness for different angles and determine σ at the value θ_L which maximizes $W(\theta)$ for the given E_{ion} and F, as an approximation of θ_c. In this process, one should make sure that all measurements are safely within the linear regime of evolution, as the onset of nonlinear effects is also nontrivially θ dependent [20].

We have taken such an approach in our experiments, with results shown in Fig. 2. Specifically, Fig. 2(a) displays the behavior of the roughness as a function of the incidence angle

for the Si(100) substrates with $E_{ion} = 0.5$ keV and 2 keV, and for the a-C substrate using $E_{ion} = 2.0$ keV, top to bottom. The corresponding $W(\theta)$ functions display maxima around $68°$, $75°$, and $75°$, respectively, which will thus be our respective estimates for θ_L. In turn, we investigate the temporal evolution of $W(t)$ fixing $\theta = \theta_L$ for each case, see Fig. 2(b). The initial data for $W(t)$ follow quite closely exponential fits of the form $W(t) = W_0 e^{\sigma t}$ (solid red lines), which yield $\sigma \simeq 0.21 min^{-1}$ for the Si targets irrespective of E_{ion}, and $\sigma \simeq 0.32 min^{-1}$ for the a-C target. These constitute our best estimates for the linear growth rate of the fastest growing Fourier mode on the unrocked substrates. Using these values and according to the results obtained in Ref. [10] given by Eq. (3), the potential optimal rocking frequencies are $0.042 min^{-1} < \nu < 0.084 min^{-1}$ for Si and $0.06 min^{-1} < \nu < 0.12 min^{-1}$ for a-C targets under the given sputter conditions.

B. 0.5 keV bombardment of Si targets

We next perform experiments at $E_{ion} = 0.5$ keV on Si targets which are rocked in a range of frequencies, from $0.017 min^{-1}$ up to $0.275 min^{-1}$, which is wider than and includes the HB-estimated range for the optimal frequency given by Eq. (3). The incident ion flux is $f = 0.625 nm^{-2} s^{-1}$, while the total ion fluence has been set to $F = 5308$ ions nm^{-2}. The results are shown in Fig. 3. Specifically, Figs. 3(a) and 3(b) show the patterns formed by IBS on unrocked surfaces at $\theta = \alpha = 62°$ and $\theta = \beta = 70°$, respectively. Then, Figs. 3(c)–3(h) show the ripple patterns produced on Si substrates which are rocked within the incidence angle interval $[\alpha, \beta]$ at various values of the rocking frequency ν, while keeping all other sputter conditions unchanged. Considering the angular diameter of the ion beam to be $3.5°$, we choose $\Delta\theta = \beta - \alpha = 8°$ to warrant well differentiated sputter effects at α and β. Recalling the $\theta_L = 68°$ value as estimated in Sec. III A for the present choice of target and ion energy, the rocking angle condition Eq. (2) seems approximately satisfied.

The corresponding 1D power spectral density (PSD) is shown below each AFM image in Fig. 3. This is computed as the PSD [21] of 1D cuts along the x axis of the 2D top view, readily allowing us to quantify the properties of the ripple patterns. Upon visual inspection of the images, the order of the patterns on the rocked surfaces in Figs. 3(c)–3(h) seems pronounced, as compared with those formed on the unrocked or stationary substrates in Figs. 3(a) and 3(b). Indeed, all the PSDs of the rocked surfaces show well-defined peaks, in sharp contrast to the stationary surfaces, whose PSD maxima are much more rounded; this indicates that rocking improves the order in the pattern for all values employed of the rocking frequency. Still, the quality of the order depends sensitively on ν. In particular, the PSD shown in Fig. 3(f) for $\nu = 9.87 \times 10^{-2} min^{-1}$ shows a markedly sharp peak.

As a quantitative measure of the order of each ripple pattern, we take the amplitude $\mathcal{A}$ and the normalized width $\Delta k/k_\circ$ of the peak in the 1D PSD, where $k_\circ$ is the wave vector of the center of the peak. Both $\mathcal{A}$ and $\Delta k/k_\circ$ are obtained by curve fitting each PSD with a Gaussian function $\mathcal{A}e^{-(k-k_\circ)^2/\Delta k^2}$ after subtracting the background, as illustrated in Fig. 3(i) for one of the PSDs, and as summarized in Fig. 3(j). Larger values of
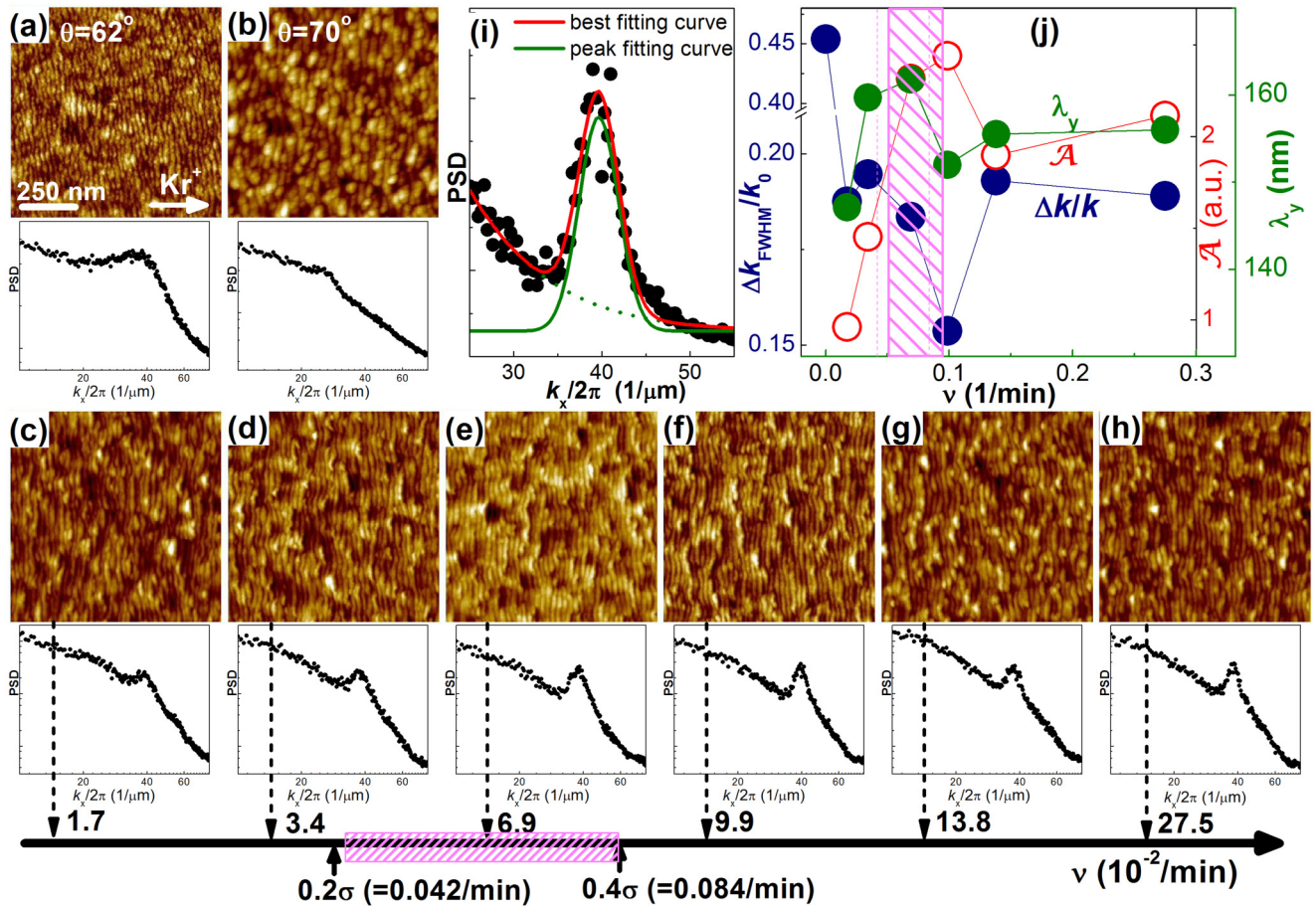
FIG. 3. Unrocked Si surfaces sputtered at (a) $\theta = 62°$ and (b) $\theta = 70°$. (c)–(h) Irradiated Si substrates rocked at frequency values ν indicated on the lower horizontal ν-scale, with $\alpha = 62° \leqslant \theta \leqslant \beta = 70°$; thus, the HB condition Eq. (2) is met, with $\Delta\theta = 8°$. In all cases, $E_{ion} = 0.5$ keV, $f = 0.625$ nm^{-2} s^{-1}, $F = 5308$ nm^{-2}, and images are 1×1 μm^2. The 1D PSD along the x axis appears below each AFM image. (i) The peak of the 1D PSD corresponding to (f) is fit by a Gaussian peak (solid green line) and background (dotted green line). The best fit of the full PSD appears as a red solid line. (j) Plot of the amplitude $\mathcal{A}$ (open symbols), normalized width $\Delta k/k_\circ$ (filled blue symbols) of the Gaussian peak, and the coherence length along the y axis λ_y (filled green symbols) as functions of the rocking frequency ν. Here, λ_y is estimated by the peak position of the 1D power spectral density along the y axis. Lines guide the eye. The pink shaded region on the ν scale below (c)–(h) and in (j) indicates the range of frequencies given by Eq. (3) using $\sigma = 0.21$ min^{-1} as obtained from the data depicted in Fig. 2(b).

$\mathcal{A}$ and smaller values of $\Delta k/k_\circ$ indicate better space ordering of the pattern [21]. Both $\mathcal{A}$ and $\Delta k/k_\circ$ show sharp extrema as a function of the rocking frequency ν, with the maximum in $\mathcal{A}(\nu)$ and the minimum in $\Delta k/k_\circ(\nu)$ being simultaneously observed around $\nu = 9.9 \times 10^{-2}$ min^{-1}. The pink-shaded region on the ν scale below Figs. 3(c)–3(h) and in Fig. 3(j) indicates the range of frequencies given by Eq. (3) using $\sigma = 0.21$ min^{-1} as obtained from the data in Fig. 2(b). As readily seen in the figure, the optimal ordering achieved in our experiments, Fig. 3(f) for $\nu = 9.87 \times 10^{-2}$ min^{-1}, occurs quite close to the upper boundary of the theoretically predicted frequency range, Eq. (3), from Ref. [10]. Actually, order also becomes optimal along the y axis under these conditions, see Fig. 3(j) for a plot of the coherence length of the ripple pattern along the y axis, λ_y, as a function the rocking frequency. Here, λ_y is estimated from the peak position of the 1D PSD along the y axis and is seen to peak around the rocking frequencies giving the best order along the x axis, indicating that rocking does improve the order of the pattern on the fully 2D surface. As

will be seen in Secs. III C and III D below, this is also the case for the two other surfaces examined. Finally, inspection of the values of $\mathcal{A}(\nu)$, $\Delta k/k_\circ(\nu)$, and λ_y at very small and very high frequencies indicates that, away from a certain range of values for ν, the substrate moves too slowly or too quickly for ripple ordering to substantially benefit from the rocking procedure.

C. 2 keV bombardment of Si targets

We further examine the predictions of HB for a higher value, $E_{ion} = 2$ keV, of the ion energy, using the same Si(100) substrate as in the previous section and $f = 0.875$ nm^{-2} s^{-1} and $F = 2182$ ions nm^{-2} for the incident ion flux and total ion fluence, respectively. For this higher energy, θ_L increases to $\theta_L \simeq 75°$ while the linear growth rate remains approximately unchanged, $\sigma \simeq 0.21$ min^{-1}, recall Figs. 2(a) and 2(b), respectively. Actually, the new value of θ_L happens to be very close to an incidence angle $\theta \simeq 80° \equiv \theta_R$, at which we observe the ripple structure on unrocked targets to change
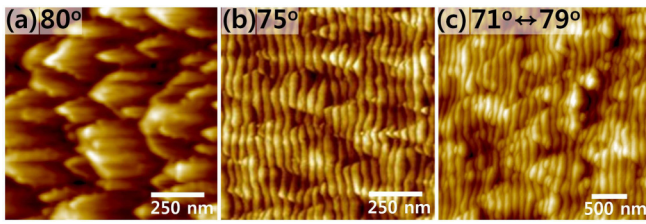
FIG. 4. Surface patterns produced on Si(100) for $E_{ion} = 2$ keV, $f = 0.875$ ions s^{-1} nm^{-2}, and $F = 2182$ ions nm^{-2}. (a) Unrocked substrate for a fixed value of the incidence angle $\theta = 80° \equiv \theta_R$. (b) Unrocked substrate for the fixed value of the incidence angle which maximizes W, $\theta_L = 75°$, as obtained from Fig. 2(a). (c) Rocked targets around θ_L, using $71° \leqslant \theta \leqslant 79°$ with $\nu = 6.9 \times 10^{-2}$/min. Both images (a) and (b) are of 1×1 μm^2, while the size of the image (c) is 3×3 μm^2.

drastically, displaying a much more complex structure along the y direction, as compared to the ripple patterns thus far discussed, see Fig. 4(a). Such an angle θ_R may perhaps correspond to the value predicted by the classic BH model at

which the ripple structure rotates by 90°, due to A' becoming negative in Eq. (1) and such that $A'(\theta) < A(\theta)$ for $\theta \geqslant \theta_R$ [2,4,14]. In any case, we consider the behavior seen at $\theta = \theta_R$ as an indication of some sort of biaxial ripple instability, frequently reported in IBS of Si targets [4]. For unrocked targets, the biaxial instability is already hinted at when irradiating for $\theta = \theta_L = 75°$, as evidenced by the severe truncation of ripples along the y direction observed on the ensuing pattern, see Fig. 4(b). If the sample is rocked around θ_L, the thus formed ripple pattern, shown in Fig. 4(c), features significant coarsening and an increased disorder, as compared with the pattern formed on a stationary substrate with the ion beam incident at θ_L, Fig. 4(b). This indicates a detrimental effect of the biaxial instability on the order of the ripple pattern and motivates us to perform rocking experiments using a reduced value for the maximum incidence angle, β, in order to stay safely away from θ_R. Accordingly, we choose $\beta < \theta_L = 75°$, specifically, we take $\alpha = 65°$ and $\beta = 73°$. Note that, as such, this rocking condition would not satisfy Eq. (2).

In contrast to the cases shown in Figs. 4(a) and 4(c), the IBS ripple patterns formed on unrocked Si substrates which
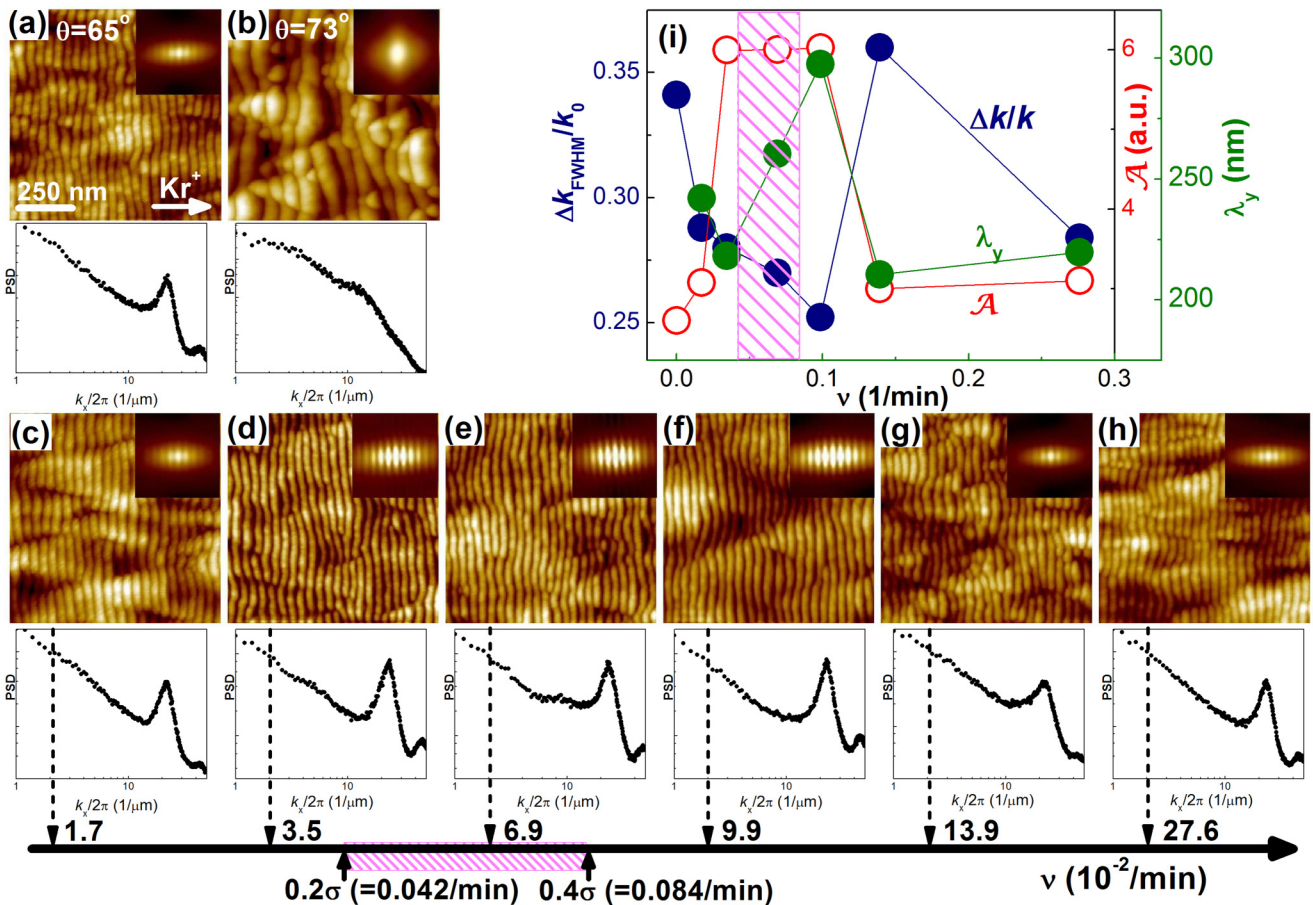
FIG. 5. Unrocked Si surfaces sputtered at (a) $\theta = 65°$ and (b) $\theta = 73°$. (c)–(h) Irradiated Si surfaces rocked at frequency values ν indicated on the lower horizontal ν scale, with $65° \leqslant \theta \leqslant 73° < \theta_L = 75°$, hence $\Delta\theta = 8°$. In all cases, $E_{ion} = 2$ keV, $f = 0.875$ s^{-1} nm^{-2}, and $F = 2182$ nm^{-2}, and images are 1×1 μm^2. For each AFM image, the 1D PSD along the x axis appears below and the inset shows the height-height correlation function. (i) Plot of the amplitude $\mathcal{A}$ (open symbols), normalized width $\Delta k/k_\circ$ (filled blue symbols) of the Gaussian peak, and the coherence length along the y axis λ_y (filled green symbols) as functions of the rocking frequency ν. Here, λ_y is estimated as in Fig. 3. Lines guide the eye. The pink shaded region on the ν scale below (c)–(h) and in (i) indicates the range of frequencies given by Eq. (3) using $\sigma = 0.21$ min^{-1} as obtained from the data depicted in Fig. 2(b).

are sputtered at $\theta = 65°$ and $\theta = 73°$ both show a somewhat mitigated biaxial instability, see Figs. 5(a) and 5(b), respectively. Also fulfilling expectations on the increase of the ripple wavelength with ion energy [20], the ripple wavelengths are now larger in Figs. 5(a) and 5(b) than those obtained on unrocked Si targets irradiated at similar angles of incidence but smaller E_{ion}, Figs. 3(a) and 3(b).

Figures 5(c)–5(h) show representative patterns formed on the rocked Si surfaces for various values of the rocking frequency ν around the range estimated in Sec. III A, under otherwise the same sputter condition as for the unrocked targets. To assess the order of the ripple patterns, we again compute the 1D PSD of each pattern, which is presented below the corresponding AFM image. From each PSD curve, both $\mathcal{A}$ and $\Delta k/k_{\circ}$ are obtained as previously described, results being summarized in Fig. 5(i). For most rocking frequencies ν, the normalized width $\Delta k/k_{\circ}$ is smaller and the amplitude $\mathcal{A}$ is larger than those of the unrocked surfaces. Hence, the rocking protocol almost invariably improves the order in the resulting pattern, as compared with the results obtained on the stationary surfaces. This is particularly clear when comparing, e.g., Fig. 5(b) for an unrocked target with what is obtained in Figs. 5(c) or 5(h) for rocking conditions under relatively low or high values of ν respectively.

The optimally ordered patterns, as defined by featuring maximum $\mathcal{A}$ and minimum $\Delta k/k_{\circ}$ values, correspond to Figs. 5(d)–5(f), as already suggested by visual inspection of both the patterns and of their height-height correlation maps [21] provided in the corresponding insets. Again, order also becomes optimal along the y axis under these conditions, see Fig. 5(i) for a plot of λ_y as a function of the rocking frequency. Remarkably, although within our angle precision Eq. (2) is not satisfied, the intermediate values of ν at which these morphologies are obtained are approximately within the interval described by Eq. (3); note, however, that the optimum condition, Fig. 5(f), appears to be already outside such frequency interval. Thus, well-ordered patterns are obtained even if the present rocking condition $\alpha < \beta < \theta_L$ *does not* imply a change in the sign of λ, which is required for order enhancement when modeled via the aKS equation [10].

D. 2 keV bombardment of a-C targets

In this section, we consider a different material, a-C, to further confirm the possibility for substrate rocking to enhance ordering of nanoripple patterns without the need of intermediate stages in which nonlinear effects cancel out, specifically that λ changes signs as expected within the description based on the aKS equation [10].

As noted above, for a-C targets using $E_{ion} = 2$ keV, it is found that $\theta_L = 75°$, see Fig. 2(a). The pattern formed by IBS of an unrocked a-C substrate at $\theta = \theta_L$ displays rectangular features as shown in Fig. 6(b), which might suggest an impending ripple reorientation transition [14,22]. Since the associated biaxial instability degrades the order of the ripple pattern very seriously, as in Sec. III C we will not rock the substrate around θ_L. In this case, we set $\beta = \theta_L$ and choose $\alpha = 67°$, so $\Delta\theta = 8°$, as for our experiments with Si substrates.

IBS of an unrocked a-C target for $\theta = \alpha$ actually leads to a well-defined ripple pattern, as shown in Fig. 6(a). Figures 6(c)–6(h) show the patterns formed on the a-C surfaces rocked at various values of ν, via IBS under otherwise the same $E_{ion} = 2$ keV sputter condition as for the stationary targets, and using $f = 0.875$ nm^{-2} s^{-1} and $F = 892$ ions nm^{-2}. Below each image, its 1D PSD is displayed, while the corresponding $\mathcal{A}$ and $\Delta k/k_{\circ}$ are shown as functions of ν in Fig. 6(i). Analogous to the previous results, ripple ordering is enhanced by rocking as compared with results on stationary targets. While such an enhancement is less pronounced for relatively low or high rocking frequencies, it becomes optimal for intermediate values of ν. Specifically, these correspond to ν between 13.8×10^{-2} min^{-1} and 17.3×10^{-2} min^{-1}, shown in Figs. 6(f) and 6(g). Such a range of values is slightly above the interval specified by Eq. (3), highlighted with color on the ν axes appearing in Fig. 6. Actually, order also becomes optimal along the y axis under these conditions, see Fig. 6(i) for a plot of λ_y as a function the rocking frequency. As is the case of the aforementioned experiments with Si, despite using a different angle interval which may differ from the one prescribed by Eq. (2), rocking again proves effective in improving the order of the pattern as compared with topographies produced on stationary targets.

E. Continuum models

Thus far, our experimental observations agree with the theoretical expectation proposed by HB [10], in the sense that rocking indeed improves spatial ordering of IBS-induced surface nanopatterns, there being a finite range of values for the rocking frequency in which order becomes optimal. However, more detailed predictions derived in Ref. [10] reach a varying degree of agreement with our experiments.

To begin, when invoking the results from Ref. [10], one is working under the assumption that the coefficients A and A' in Eq. (1) do not change under rocking. Actually, HB also discuss the (more realistic) alternative possibility that, in our notation, $A(\alpha) \neq A(\beta)$, showing that although such a behavior may be detrimental to the quality of the pattern, order improvement can still be achieved for suitable parameter choices. As the detailed discussion provided on this aspect in Ref. [10] corresponds to rocking of 1D substrates, we have performed numerical simulations of the full 2D aKS equation, Eq. (1), to confirm the generality of such a conclusion for the physically more realistic case of 2D rocking target surfaces. In all our numerical simulations, we have employed a finite-difference discretization scheme in space (with lattice spacing $\delta x = 0.5$) and a fourth-order Runge-Kutta algorithm for the time evolution (using time step $\delta t = 2 \times 10^{-4}$), and periodic boundary conditions, as, e.g., in Ref. [23]. As an initial condition, we employ uncorrelated, Gaussian random noise with a small amplitude of order 10^{-2} in the nondimensional units employed, while we have checked that results to not change appreciably for other values of δx and δt.

Sample results of our numerical simulations of Eq. (1) are shown in Fig. 7. These correspond to different putative (continuous) rocking protocols for each of which, not only $\lambda(\alpha) \neq \lambda(\beta)$, but also $A(\alpha) \neq A(\beta)$. The right column of the figure corresponds to ranges of values for λ in which,
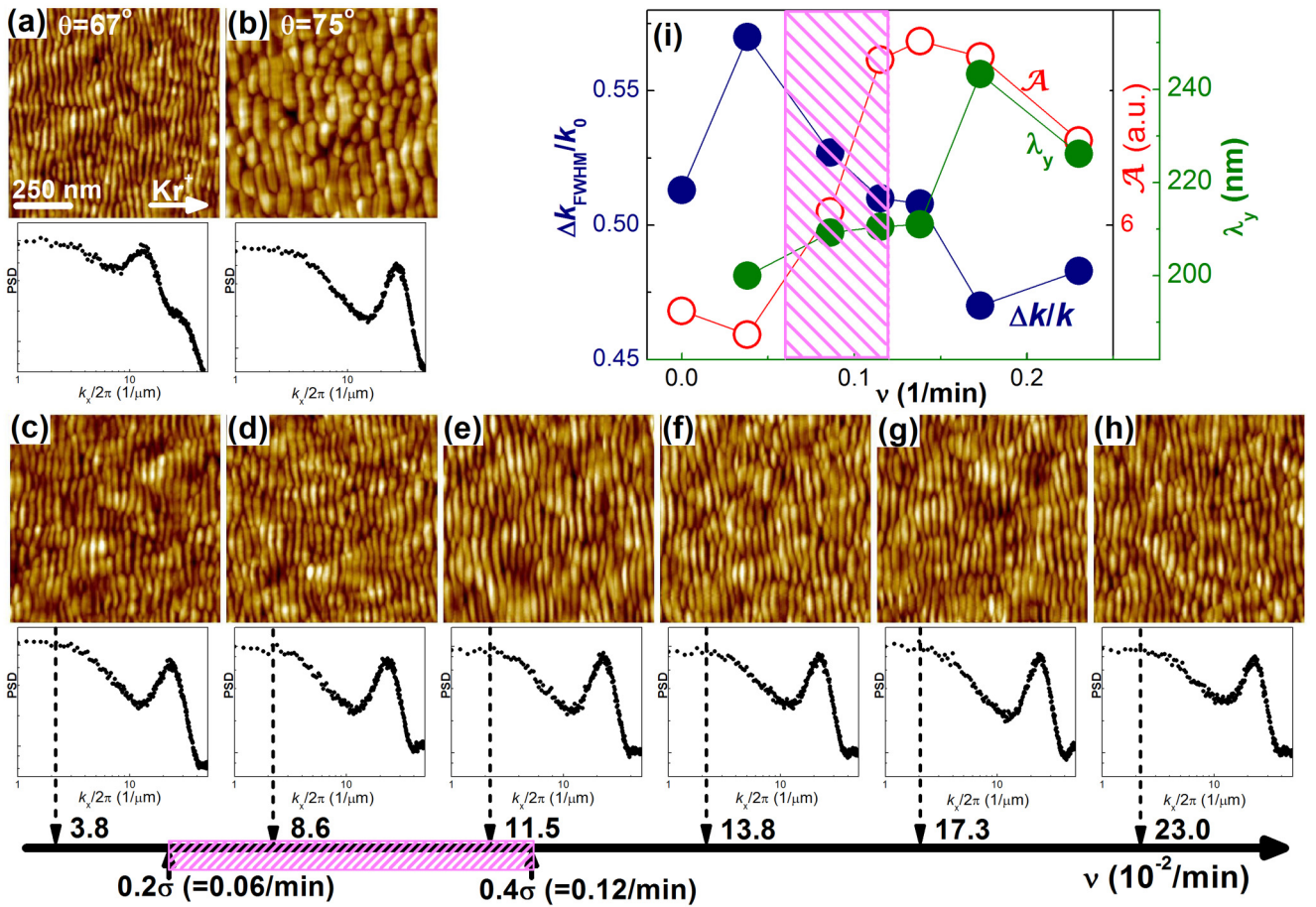
FIG. 6. Unrocked a-C surfaces sputtered at (a) $\theta = 67°$ and (b) $\theta = 75°$. (c)–(h) Irradiated a-C surfaces rocked at frequency values ν indicated on the lower horizontal ν scale, with $\alpha = 67° \leqslant \theta \leqslant \beta = \theta_L = 75°$, hence $\Delta\theta = 8°$. In all cases, $E_{\mathrm{ion}} = 2$ keV, $f = 0.875$ nm^{-2} s^{-1}, and $F = 892$ nm^{-2}, and images are 1×1 μm^2. For each AFM image, the 1D PSD along the x axis appears below. (i) Plot of the amplitude $\mathcal{A}$ (open symbols), normalized width $\Delta k/k_\circ$ (filled blue symbols) of the Gaussian peak, and the coherence length along the y axis λ_y (filled green symbols) as functions of the rocking frequency ν. Here, λ_y is estimated as in Fig. 3. Lines guide the eye. The pink shaded region on the ν scale below (c)–(h) and in (i) indicates the range of frequencies given by Eq. (3) using $\sigma = 0.32$ min^{-1} as obtained from the data depicted in Fig. 2(b).

although $\lambda(\alpha) \neq \lambda(\beta)$, this parameter does not change signs. As expected from Ref. [10], no improvement in surface ordering takes place, the corresponding ripple arrangements being quite disordered, as generally expected for the aKS equation at long times in large spatial domains [11–13]. In contrast, in the left column in Fig. 7, where conditions are such that λ does change sign under rocking, virtually perfect order is always observed when ν is close to the theoretically predicted optimum [10] in spite of the fact that, say, $A(\alpha) = 0.5 \neq 1.0 = A(\beta)$. Here, $A(\alpha)$ and $A(\beta)$ are chosen to reflect the difference in the ripple wavelengths of the patterns on the stationary substrates sputtered at $\theta = \alpha$ or $\theta = \beta$. We have checked in additional simulations (see Appendix B) that the specific numerical values of the parameters do not play a relevant role in this qualitative behavior, which seems to be quite generic for Eq. (1). Moreover, a general trend is observed (see again Appendix B), such that an increase in the difference between $A(\alpha)$ and $A(\beta)$ implies a decrease of the range of rocking frequencies producing virtually perfect order.

Considering our experiments on Si at $E_{\mathrm{ion}} = 0.5$ keV, the overall agreement with the HB picture of rocking seems substantial. Indeed our experiments, being consistent with the angle condition prescribed by Eq. (2), lead to optimal ripple ordering when rocking proceeds at a frequency (almost) within the theoretically predicted interval given by Eq. (3), recall Fig. 3. To date, the precise dependence of the coefficient λ appearing in the aKS equation with the incidence angle θ is not well known. Explicit formulas are available in Ref. [1], which were derived by extending to nonlinear order Bradley and Harper's results [14] on the dependence of the local erosion rate on the local surface geometry, according to Sigmund's classic description of energy deposition from collision cascades [3,4]. To apply the result from Ref. [1], knowledge is in turn required on the average ion penetration depth and the lateral stragglings of the assumed Gaussian distribution of energy deposition. Simulations (not shown) using the Stopping and Range of Ions in Matter (SRIM) package [24] yield 8.2 nm, 2.6 nm, and 2.4 nm values, respectively, for these parameters which, once fed into the
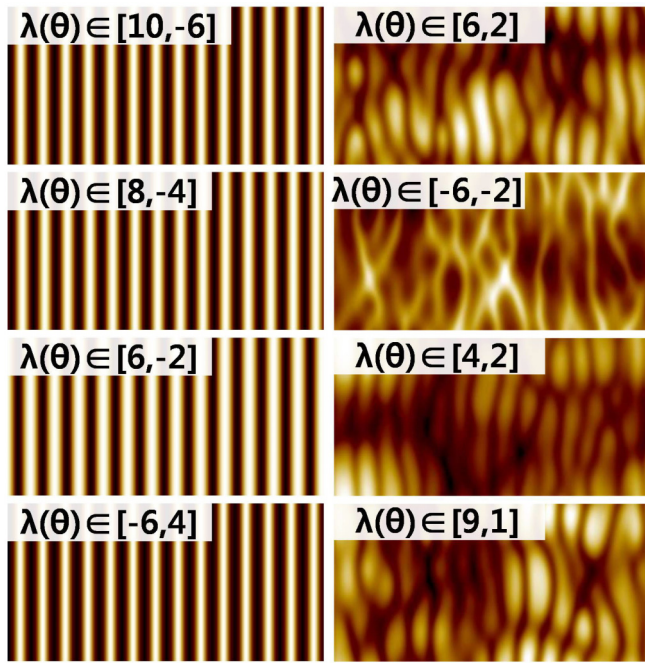
FIG. 7. Top views of surface morphologies obtained from numerical simulations of the 2D aKS equation, Eq. (1), at steady state for $A' = 1.0$, $B = 1.0$, and $\lambda' = 2$. The parameters A and λ change periodically in the $[A(\alpha), A(\beta)] = [0.5, 1.0]$ and $[\lambda(\alpha), \lambda(\beta)]$ intervals, respectively, with the latter being specified on each panel. The rocking frequency employed, $\nu = 0.04$, corresponds to Harrison and Bradley's estimate, Eq. (5) [10], where we have used $A = (A(\alpha) + A(\beta))/2 = 0.75$. All units are arbitrary.

FIG. 8. PSD of 1D interfaces at steady state from numerical simulations of (a) and (b) the 1D (no y dependence) aKS equation, Eq. (1), and (c) the 1D (no y dependence) eaKS equation, Eq. (6), under rocking conditions such that $\lambda \in [\lambda(\alpha), \lambda(\beta)]$, with intervals as indicated in each panel. The rocking frequency $\nu = 0.075$ in all cases. The remaining parameter values are $A = 1$ and $B = 1$. All units are arbitrary.

expression for $\lambda(\theta)$ [1], predicts $\theta_c^{\mathrm{SRIM}} \simeq 65°$ as the incidence angle at which the corresponding nonlinear term cancels out. This value is not far from the $\theta_L \simeq 68°$ value estimated from the experiments reported in Sec. III C. In view of the many approximations involved in this calculation and of our angular uncertainties, the proximity between these two values may be even coincidental, but is still suggestive of the applicability of the aKS equation to our experiments on Si with $E_{\mathrm{ion}} = 0.5$ keV. We would like to note that the expressions for, e.g., the linear-term coefficients A and A' derived in Ref. [1] are known not to be correct, as they predict pattern formation for $\theta = 0°$ under the present conditions, which contradicts observations, see Ref. [4] and references therein for a detailed discussion.

Our experimental results for Si at higher energy ($E_{\mathrm{ion}} = 2$ keV) or with a-C targets contrast, however, with our results on Si at $E_{\mathrm{ion}} = 0.5$ keV, from the point of view of their comparison with predictions by the aKS equation under rocking conditions. While experimental errors affect the determination of θ_L and the extent to which θ_L approximates the θ_c value at which $\lambda(\theta_c) = 0$ in the aKS equation, the systems addressed in Secs. III C and III D may not satisfy Eq. (2), under which rocking is predicted by the aKS equation to enhance ordering. And while our 2 keV rocking experiments do achieve order improvement for a finite range of ν values, as expected from the point of view of the aKS equation, the optimal frequency seems to overshoot the aKS-predicted range more clearly than in our 0.5 keV results. Note that the above-predicted range

assumes A is θ independent. If we allow A to change during rocking as the experimental observation indicates, the overshooting increases further, since the optimal rocking range narrows as found in Fig. 11(b). Recall that Eq. (2) stems from the condition that λ changes signs during rocking. Figure 8(a) shows the surface PSD from a numerical simulation (in which the y dependence has been dropped, for simplicity) of the aKS equation, Eq. (1), under rocking such that λ does not change signs. Indeed, the broad peak of the PSD speaks of quite a disordered ripple structure. Quite a different result is seen in Fig. 8(b), where a sharp peak (nearly perfect order) is obtained under rocking such that λ changes signs, also according to Eq. (1). These behaviors suggest that the aKS equation may not properly describe our experimental observation for Si with $E_{\mathrm{ion}} = 2$ keV or for a-C targets.

Looking for further theoretical support for our experimental observations, we find that the interface equation

$$h_t = -Ah_{xx} + A'h_{yy} - B\nabla^4 h + \frac{\lambda}{2}h_x^2 + \frac{\lambda'}{2}h_y^2$$
$$+ r\nabla^2\left(\frac{\lambda}{2}h_x^2 + \frac{\lambda'}{2}h_y^2\right) \tag{6}$$

is quite informative. Equation (6) is a minimal generalization of the aKS model (which is readily retrieved for $r = 0$) via the additional nonlinear term proportional to parameter r, thus being a particular anisotropic generalization of the so-called extended KS (eKS) equation, which we will term the eaKS equation. Being consistent with a conservation-law form for the height equation as $h_t = -\nabla \cdot \mathbf{J}$ for $\mathbf{J} =$

$-r\nabla(\lambda h_x^2/2 + \lambda' h_y^2/2)$, this additional nonlinearity preserves the total amount of material and is frequently described as a (anisotropic) conserved KPZ term [13]. In the IBS context, the $\lambda = \lambda'$ isotropic limit of this term has been proposed to describe the contribution of irradiation to surface-confined transport, rather than sputtering, of material, yielding the so-called eKS equation for the height, in which $A = A'$ as well [6,16,25]. The eKS equation has been shown to have predictive power when compared to experiments under normal ion incidence ($\theta = 0°$) on, e.g., interrupted ripple coarsening on Si [17] or on nanobead formation on Au by sequential IBS [23,26]. Under oblique irradiation conditions, the eKS model becomes anisotropic [27,28]; further generalizations of it can be formulated [29] to describe IBS systems in the presence of, e.g., preferential transport along specific substrate directions and/or strong surface tension anisotropies.

In our present context, we view Eq. (6) as a means to incorporate to the aKS equation additional (nonlinear) effects due to surface-confined transport, which are expected to be particularly relevant for IBS of semiconductor targets at low-to-medium ion energies [4]. Indeed, amorphization of a near-surface layer by irradiation and viscous relaxation of such layer have been shown [30] to account for many early-time properties of ripple formation in this class of systems (see additional references, e.g., in Ref. [4]). The most relevant nonlinearities induced by these relaxation processes have been recently elucidated [31], indicating a highly complex interplay among various terms, all of which are conservative. Hence, we presently take the eaKS model as a minimal model representing the *nonlinear* competition between conservative effects, like ion-induced amorphization and viscous flow (via the conserved KPZ terms), and non-conservative effects, e.g., sputtering, represented by the KPZ nonlinearities.

We have performed numerical simulations of Eq. (6) in the context of substrate rocking. Already for 1D surfaces, Fig. 8(c) shows that the eaKS equation can describe surfaces with improved order (the PSD features several sharp peaks) under rocking conditions such that λ does not change signs. Analogous conclusions are obtained in the full 2D case, addressed in Fig. 9. This figure compares simulations of the eaKS equation, Eq. (6) (left column), with simulations of the aKS equation obtained setting $r = 0$ in Eq. (6), Eq. (1) (right column), and otherwise identical parameter conditions. We have also checked different parameter values—such that $r < 0$ at all times, thus guaranteeing absence of nonlinear instabilities [32]—and rocking frequencies, with the same qualitative conclusions, see Appendix C. As is clear from Fig. 9, the eaKS equation, Eq. (6), predicts (panels on the left column) order improvement even in cases for which $A(\alpha) \neq A(\beta)$, and generically better ordering as compared with the aKS equation under the same parameter conditions (panels on the right column). What is particularly remarkable is that the eaKS equation predicts order improvement under rocking even when the KPZ coefficient λ does *not* change signs during the rocking protocol, irrespective of its fixed sign, whether positive or negative. Hence, from the point of view of the description of IBS via Eq. (6), the rocking procedure does not require intermediate steps in which nonlinear effects cancel, to induce order improvement. In this sense, the eaKS equation seems qualitatively consistent with our experimental results at
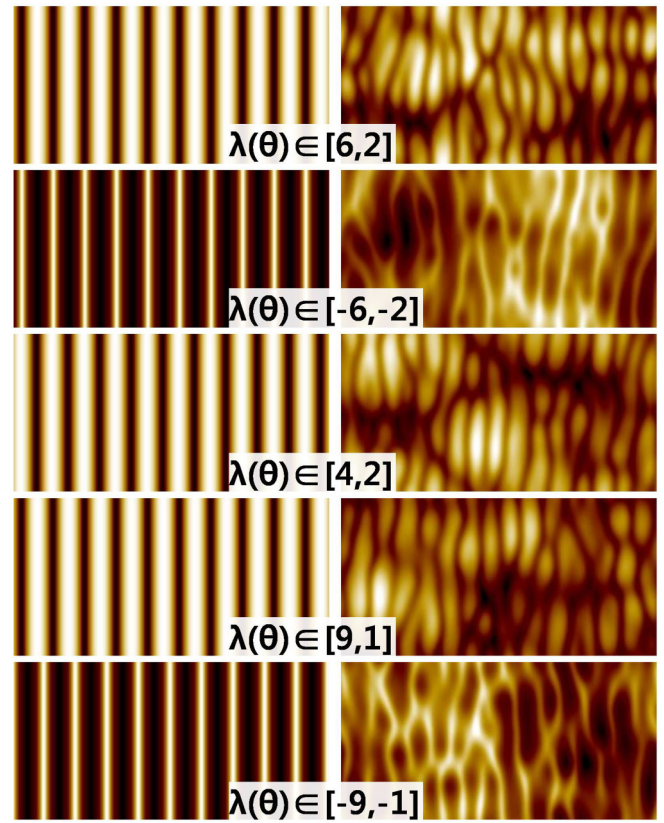
FIG. 9. Left column: Top views of surface morphologies obtained from numerical simulations of the eaKS equation, Eq. (6), at steady state, for $A' = 1$, $B = 1$, $\lambda' = 2$, and $r = -5$. The parameters A and λ change periodically in the $[A(\alpha), A(\beta)] = [0.5, 1.25]$ and $[\lambda(\alpha), \lambda(\beta)]$ intervals, respectively, with the latter being specified on each panel. Right column: Same as left column but for the aKS equation, Eq. (1), i.e., setting $r = 0$ in each case. The rocking frequency employed, $\nu = 0.055$, corresponds to Harrison and Bradley's estimate, Eq. (5) [10], where we have used $A = (A(\alpha) + A(\beta))/2 = 0.88$. All units are arbitrary.

$E_{ion} = 2$ keV for Si and for a-C, in which rocking enhances ordering in spite of the fact that the angle condition, Eq. (2), may not hold.

A remaining question is then why the experimental observations on Si for $E_{ion} = 0.5$ keV are elucidated well by the aKS model, while those with $E_{ion} = 2$ keV request additional nonlinear effects like those represented by the (anisotropic) conserved KPZ (cKPZ) term. A rationale is that the surface-confined transport mechanism represented by this term becomes more relevant by increasing the value of E_{ion} [16]. Thus, for $E_{ion} = 0.5$ keV viscous flow (hence, the cKPZ term) is less relevant to describe the pattern formation process during rocking, which would be more dominated by sputtering-related nonlinearities like the ones described by the aKS equation, while the converse would happen for the higher ($E_{ion} = 2.0$ keV) condition. Actually, this is the case experimentally for Ar^+ irradiation of Si [33]: while ripples form at suitable incidence angles for $E_{ion} = 0.5$ keV, they do not form at any angle at $E_{ion} = 3$ keV, as a result of the increased relevance of (conservative) mass redistribution processes at the surface at the higher energy condition [33]. From this point

of view, all our experiments would be described by Eq. (6), although those performed at 0.5 keV would correspond to a value of r which is so small that the behavior can be described effectively by the aKS equation [34].

IV. DISCUSSION

Given the fact that the starting unirradiated targets are crystalline in all our experiments, in principle one might naturally expect some influence of crystallinity on the quality of the ordering of the obtained nanopatterns. However, e.g., low-energy Kr^+ or Xe^+ irradiation of Si and a-C [35] are well known to induce formation of a thin amorphized layer at the free interface, whose thickness is of the order of the ion range [36], and which controls the pattern formation process, irrespective of the initial condition (whether crystalline or amorphous) of the target [30,37]. Hence, we do not expect that the target crystallinity influences significantly the pattern order properties observed in Secs. III B–III D.

In absence of crystallinity effects, as assumed in Sec. III E, Carter [38] also studied theoretically the effects of substrate rocking, but without taking nonlinear effects into account, and found no improvement in the order of the pattern being induced by rocking, in sharp contrast to our present experimental observations. This points to the significant role of the modulation of nonlinear effects in the improvement of the order of the patterns formed on the rocked surface by IBS.

Actually, in the nonlinear aKS equation, the rocking procedure does induce some type of modulation of the relative importance of nonlinear effects with respect to linear effects. From this fact, HB [10] suggested a heuristic picture for such a modulation: while linear effects dominate the surface evolution, the Fourier spectrum of the surface height becomes narrower around the most dominating mode corresponding to the ripple structure. This acts as a filtering process, with the consequence of an improvement of the pattern order as IBS proceeds. However, the nonconserved KPZ nonlinearity interrupts this process, as it efficiently leads to amplitude saturation [1,11,16,17]. Hence, order improvement via rocking requires $\lambda = 0$ at intermediate stages in the rocking cycle. Conversely, large values of $|\lambda|$ in Eq. (1) induce smaller ripple amplitudes.

In the present paper, we elucidate further nonlinear effects in IBS patterns during rocking. We observe experimentally that substrate rocking can also enhance the order under angle conditions which may violate Eqs. (2) and (3). This observation implies that the nonlinear aKS model may not suffice to explain all experimental observations. A minimal enhancement of the aKS equation by the introduction of additional cKPZ nonlinearities as in the eaKS equation, Eq. (6), seems to more completely account for experimental observations. Now, for non-negligible values of r, the condition that $\lambda = 0$ is not needed during rocking to improve surface order. We rather believe that ordering emerges in the eaKS equation as a competition between different nonlinear effects. Indeed, in the eKS equation [34,39,40], the cKPZ nonlinearities are known to act at smaller length and timescales than KPZ nonlinear terms. In the presence of a linear instability, the former tend to coarsen the ensuing pattern, both in wavelength and in amplitude, a process which is eventually interrupted by

the nonconserved nonlinearities for sufficiently large scales. Actually, such a competition is able to introduce short-range order for suitable parameter choices [29,34,39,40]. In general, we expect the relative strength of the two nonlinear terms in Eq. (6), which is determined by the substrate and the sputter conditions, to dictate the optimal rocking condition for the improvement of the patterns. Moreover, as suggested, e.g., by the morphology shown in Fig. 4(a), one can expect additional nonlinear effects, as, e.g., those ensuing from refined descriptions of sputtering [41,42] and of surface-confined viscous flow [4,31] to improve the quantitative description of IBS under substrate rocking for semiconductor targets.

In our experiments, we have also seen that the pattern order depends sensitively on the rocking frequency ν under otherwise the same sputter conditions. The location of the optimal range for ν determined by the experiment is found within or near the one derived theoretically from the aKS equation [10]. Their proximity may be fortuitous, since the present rocking experiments are not generally performed as prescribed by this theoretical description. At any rate, $1/\sigma$ still provides a characteristic time scale comparable to the rocking period, and the optimal range of frequencies is thus anticipated to be determined by σ. If this is the case, the theoretically predicted optimal range of rocking frequencies would serve well as a guide to investigate the corresponding range in experiments.

Even the best ordered patterns observed in Figs. 3, 5, and 6 commonly show a varying density of residual linear defects and peculiar triangularlike structures which run at specific angles to the k-vector direction of the ripple pattern. These defects have been previously reported, for instance, on sputtered Si(100) [20,43,44] and have been recently attributed to the broken mirror symmetry implied by the ion incidence [45]. If this is the case, one possibility to remove these defects and further improve surface order would be rocking the substrate while preserving the mirror symmetry on the target plane, e.g., by alternating rocking between α and β and between $-\alpha$ and $-\beta$ [46]. Such further improvement of the order in the pattern should be an interesting extension of the present paper and will be addressed elsewhere.

V. SUMMARY AND CONCLUSION

We have examined experimentally whether substrate rocking during IBS can improve the order in the nanoripple patterns produced by this technique, as theoretically proposed by HB [10]. For Si(100) sputtered by Kr^+ with $E_{ion} = 0.5$ keV, pattern improvement by rocking is indeed observed for an optimal rocking frequency which, albeit not in the predicted range, is quite close to it. A number of additional experimental properties are fairly well described by the original theoretical proposal via the aKS equation, Eq. (1).

For Si(100) and a-C sputtered for $E_{ion} = 2$ keV, we also find improvement of the pattern by substrate rocking. However, the theoretically prescribed [10] rocking condition, Eq. (2) [stemming from requiring that λ in Eq. (1) should change signs during the rocking cycle], may not be met in these cases. Moreover, the optimal rocking frequency values somewhat overshoot the theoretically predicted range. Building upon these observations, we consider the extended aKS
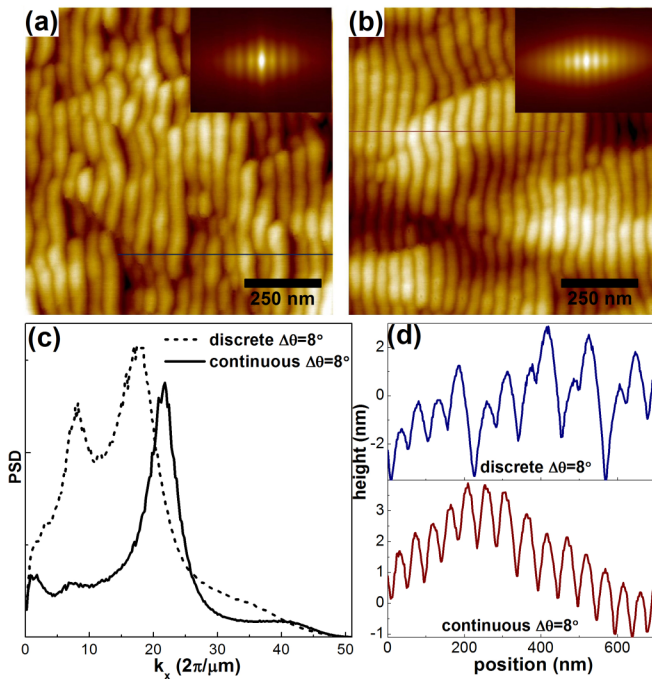
FIG. 10. (a) *Discretely*, and (b) *continuously* rocked Si(100) target undergoing IBS under the same conditions: $\alpha = 65°$, $\beta = 73°$, $\nu = \nu_\circ = 6.91 \times 10^{-2}$ min^{-1}, $E_{ion} = 2$ keV, $f = 0.813$ ions nm^{-2} s^{-1} (normal to the surface), and $F = 2182$ ions nm^{-2}. The size of both top-view AFM images is 1×1 μm^2. The inset in each image shows its height-height correlation function. (c) 1D PSD of $\partial h/\partial x$ for both (a) and (b). (d) Top and bottom panels show representative line profiles along the solid lines parallel to the x axis in (a) and (b), respectively.

model, Eq. (6), which generalizes the previously employed anisotropic KS equation by introducing additional conserved KPZ nonlinearities, which may be particularly appropriate for semiconductor targets. This allows us to still reproduce order improvement, even if λ does not necessarily change signs, as one might expect for these experimental conditions. This supports the eaKS model as a comprehensive, albeit minimal, model to understand the mechanisms by which rocking improves the order of the nanopatterns.

APPENDIX A: CONTINUOUS VS DISCRETE ROCKING

Figure 10 shows the surface ripple pattern formed by IBS of a Si(100) target which is either discretely [panel (a)] or continuously [panel (b)] rocked for incidence angles θ between $\alpha = 65°$ and $\beta = 73°$, at a rocking frequency $\nu_\circ = 6.91 \times 10^{-2}$ min^{-1}, and using Kr$^+$ ions with $E_{ion} = 2$ keV. All additional sputter conditions are also the same for the two different rocking experiments. Visual inspection of the images already suggests that better order is achieved in the case of continuous rocking. The height-height correlation map of the top-view images supports this conclusion, as the continuously rocked surface displays a substantially longer correlation length than the discretely rocked surface, compare the insets of Figs. 10(a) and 10(b).

Figure 10(c) shows the 1D PSDs along the x axis of the patterns displayed in Figs. 10(a) and 10(b). To enhance pattern features, the derivative of the height field $h(x, y)$ along the x axis is previously computed for each image, and the 1D PSD is computed for the resulting image. For the discretely rocked surface, the thus computed 1D PSD shows two pronounced peaks. The wavelength which corresponds to the main peak with the larger wave-vector value, i.e., $\lambda_K = 58.5$ nm, is similar to the correlation length obtained from the height-height correlation function, namely 57 nm, see the inset of Fig. 10(a). This length scale thus originates from the average ripple period and constitutes the fundamental wavelength of the pattern. On the other hand, the wavelength which corresponds to the smaller wave-vector peak of the 1D PSD, $\lambda_k = 117$ nm, is about $2\lambda_K$. Indeed, paired ripples abound in the pattern as noticed in the representative line profile shown in Fig. 10(d) (top). Hence, discrete rocking seems to drive an additional instability of the ripple pattern, leading to coarsening of the morphology via pairing of adjacent ripples.

In contrast, the 1D PSD of the ripple pattern shows no such conspicuous additional peak for the continuously rocked surface, but only a minor one as shown in Fig. 10(c). In this case, ripples show little, if any, pairing in the corresponding representative line profile in Fig. 10(d) (bottom). Now the mean wavelength $\lambda_K = 46.5$ nm, as estimated from the peak position in the 1D PSD, a value which is notably smaller than the 58.5 nm value obtained for the discretely rocked surface. The surface width or roughness, $W \simeq 1.90$ nm, is also smaller for the case of continuous rocking than for the discretely rocked surface, for which $W \simeq 2.66$ nm. Moreover, ripples show many less interruptions along the y direction in the former than in the latter case. Thus, the rocking protocol (continuous vs discrete) is found to make a substantial difference with respect to the quality of the ripple pattern.

Considering the sizable long-wavelength height modulation which is observed on stationary (unrocked) surfaces sputtered at $\beta = 73°$ [see Fig. 5(b)], the observed coarsening via ripple pairing in the discrete rocking case can be attributed to the extended sputtering which takes place with $\theta = \beta$ during each discrete rocking period. In turn, the relatively large W which also ensues under discrete rocking conditions can also be attributed to such a height modulation. In the case of continuous rocking, IBS mostly takes place away from the $\theta = \beta$ condition, the height modulation contributes less to the overall pattern, and the peak at the smaller wave vector in the 1D PSD is much less pronounced than that for the discrete rocking, as shown in Fig. 10(c).
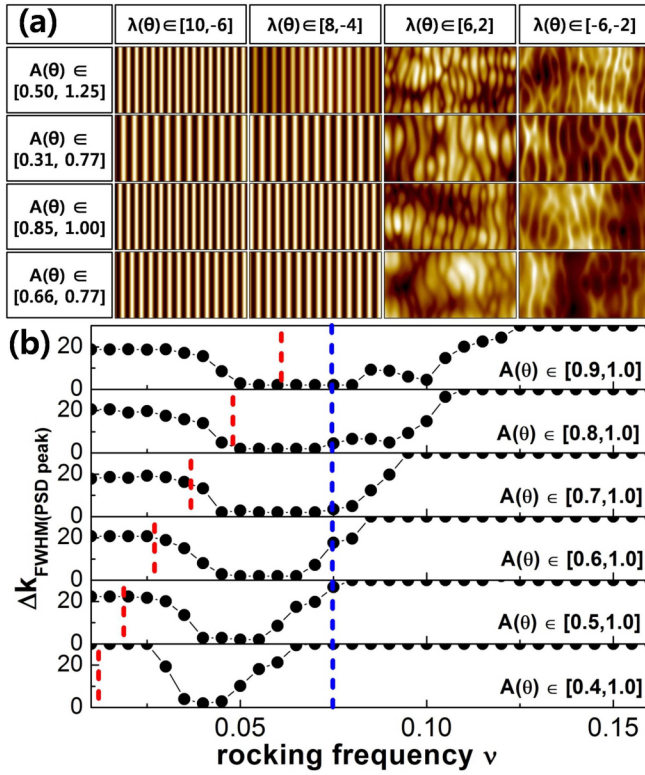
FIG. 11. (a) Ripple patterns for different $[\lambda(\alpha), \lambda(\beta)]$ and $[A(\alpha), A(\beta)]$ combinations, from numerical simulations of the aKS equation, Eq. (1). Here, $A' = 1.0$, $B = 1.0$, and $\lambda' = 2$. Only when $\lambda(\alpha) \cdot \lambda(\beta) < 0$ can virtually perfect patterns form, irrespective of $[A(\alpha), A(\beta)]$. (b) The full width at half maximum (FWHM) of the PSD peak associated with each 1D pattern, Δk_{FWHM}, is plotted as a function of the rocking frequency ν for different $[A(\alpha), A(\beta)]$, while $B = 1.0$ and $\lambda(\theta) \in [10, -6]$. The optimal range of ν giving the minimal Δk_{FWHM} narrows as the difference between $A(\alpha)$ and $A(\beta)$ increases and is found around the theoretically predicted range demarcated by the vertical dashed lines. Specifically, the red (blue) line indicates the frequency value given by Eq. (5), assuming $A(\theta)$ to be constant and equal to $A(\alpha)$ ($A(\beta)$).

In short, during discrete rocking two distinct instabilities caused by IBS at the limiting angles, α and β, are alternatively at work, which adversely impact the quality of the resulting ripple pattern. No such behavior seems to take place during continuous rocking; consequently, the pattern order on discretely rocked surfaces is substantially poorer than the order achieved under continuous rocking conditions.

APPENDIX B: PREDICTIONS OF THE AKS MODEL FOR VARIOUS PARAMETER CONDITIONS

Figure 11(a) shows the simulated patterns on the continuously rocked surface according to the aKS model for various combination of $[A(\alpha), A(\beta)]$ and $[\lambda(\alpha), \lambda(\beta)]$. It plainly tells that the virtually perfect pattern can be fabricated only if $\lambda(\alpha) \cdot \lambda(\beta) < 0$, irrespective of the $[A(\alpha), A(\beta)]$ interval employed. Figure 11(b) shows the full width at half maximum (FWHM) of the PSD peak, Δk_{FWHM}, associated with each 1D pattern for different $[A(\alpha), A(\beta)]$ as a function of ν, while $\lambda(\alpha) \cdot \lambda(\beta) < 0$. By increasing the difference between $A(\alpha)$
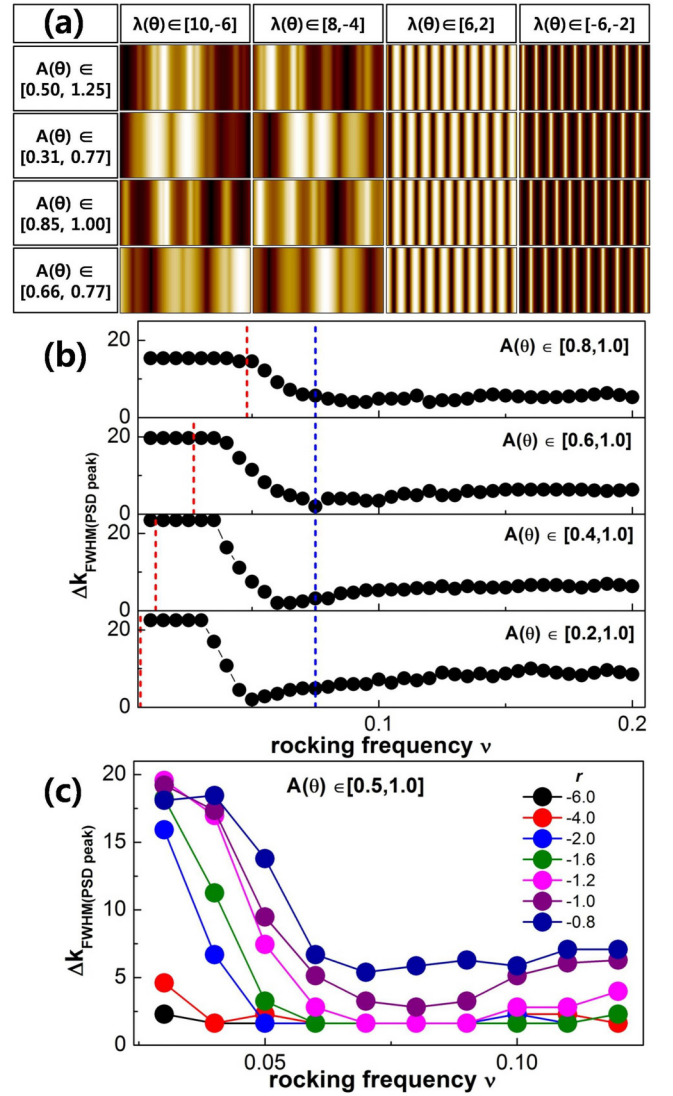
FIG. 12. (a) Ripple patterns for different combination of $[\lambda(\alpha), \lambda(\beta)]$ and $[A(\alpha), A(\beta)]$, from numerical simulations of the aeKS equation, Eq. (6), using $A' = 1.0$, $B = 1.0$, $\lambda' = 1.0$, and $r = -5$. Only when $\lambda(\alpha) \cdot \lambda(\beta) > 0$ do the highly ordered patterns form. (b) The full width at half maximum (FWHM) of the main PSD peak from the respective 1D pattern, Δk_{FWHM}, is plotted as a function of the rocking frequency for different $[A(\alpha), A(\beta)]$s, while $B = 1.0$, $r = -1$, and $\lambda(\theta) \in [6, 2]$. Both, the minimal Δk_{FWHM} and the optimal frequency range depend nontrivially on $[A(\alpha), A(\beta)]$. The ν value yielding the minimal Δk_{FWHM} is still around the theoretically predicted range: the red (blue) line indicates Harrison and Bradley's [10] estimate of the optimal frequency, Eq. (5), when $A(\theta)$ is equal to $A(\alpha)$ [$A(\beta)$]. (c) Δk_{FWHM} of the 1D pattern is plotted as a function ν for different values of r, while $B = 1.0$, $A(\theta) \in [0.5, 1]$, and $\lambda(\theta) \in [6, 2]$. As the magnitude of r increases, the minimal Δk_{FWHM} decreases and the optimal range of ν increases, indicating the significant role of the cKPZ term in strengthening the order of the pattern.

and $A(\beta)$, the optimal range of ν producing the minimal Δk_{FWHM} decreases. For each $[A(\alpha), A(\beta)]$ interval, the optimal range of ν still stays near the predicted optimal range of ν that is demarcated by the vertical dashed lines in Fig. 11(b).

Specifically, the red and blue lines indicate HB's [10] estimate of the optimal frequency, Eq. (5), when $A(\theta)$ is assumed constant and equal to, respectively, $A(\alpha)$ and $A(\beta)$.

APPENDIX C: PREDICTIONS OF THE AEKS MODEL FOR VARIOUS PARAMETER CONDITIONS

Figure 12(a) shows simulated patterns according to the aeKS model for various combination of the $[A(\alpha), A(\beta)]$ and $[\lambda(\alpha), \lambda(\beta)]$ intervals. In sharp contrast to the aKS model, only if $\lambda(\alpha) \cdot \lambda(\beta) > 0$ can the virtually perfect pattern develop. Figure 12(b) shows Δk_{FWHM} of the 1D pattern as a function of ν for various $[A(\alpha), A(\beta)]$ intervals, while $\lambda(\alpha) \cdot \lambda(\beta) > 0$. As ν increases, Δk_{FWHM} drops down to a poorly defined minimum in a very narrow range of ν. However, while Δk_{FWHM} does increase for still larger ν, the Δk_{FWHM} values remain quite small for a wide range of ν, leading to substantial order enhancement as compared with the unrocked surface. Such a ν dependence of Δk_{FWHM} is commonly observed, irrespective of $[A(\alpha), A(\beta)]$, while the minimal Δk_{FWHM} marginally decreases as the difference between $A(\alpha)$ and $A(\beta)$ increases. The minimal Δk_{FWHM} is also found near the theoretical optimal range of ν demarcated by the red and blue vertical lines in Fig. 12(b), as is the case for the aKS model shown in Fig. 11(b).

Figure 12(c) shows the ν dependence of Δk_{FWHM} for different values of r. As the magnitude of r increases, the minimal Δk_{FWHM} decreases and the optimal range of ν giving the minimal Δk_{FWHM} increases, indicating the significant role of the cKPZ term in strengthening the order in the ripple pattern. In our present experiments with both Si and a-C, $\Delta k_{\mathrm{FWHM}}(\nu)$ commonly shows a well-defined minimum in a narrow range of ν, see Figs. 3, 5, and 6, similar to the $r \simeq -1$ behavior shown in Fig. 12(c).

[1] M. Makeev, R. Cuerno, and A.-L. Barábasi, Nucl. Instrum. Methods Phys. Res., Sect. B **197**, 185 (2002).

[2] W. L. Chan and E. Chason, J. Appl. Phys. **101**, 121301 (2007).

[3] J. Muñoz-García, L. Vázquez, R. Cuerno, J. A. Sanchez-García, M. Castro, and R. Gago, in *Toward Functional Nanomaterials*, edited by Z. Wang (Springer, New York, 2009), pp. 323-398.

[4] J. Muñoz-García, L. Vázquez, M. Castro, R. Gago, A. Redondo-Cubero, A. Moreno-Barrado, and R. Cuerno, Mater. Sci. Eng., R **86**, 1 (2014).

[5] S. Facsko, T. Dekorsy, C. Koerdt, C. Trappe, H. Kurz, A. Vogt, and H. L. Hartnagel, Science **285**, 1551 (1999).

[6] T. C. Kim, C.-M. Ghim, H. J. Kim, D. H. Kim, D. Y. Noh, N. D. Kim, J. W. Chung, J. S. Yang, Y. J. Chang, T. W. Noh, B. Kahng, and J.-S. Kim, Phys. Rev. Lett. **92**, 246104 (2004).

[7] C. S. Madi, H. B. George, and M. J. Aziz, J. Phys.: Condens. Matter **21**, 224010 (2009).

[8] J.-H. Kim, M. Joe, S.-P. Kim, N.-B. Ha, K.-R. Lee, B. Kahng, and J.-S. Kim, Phys. Rev. B **79**, 205403 (2009).

[9] A. Keller and S. Facsko, Phys. Rev. B **82**, 155444 (2010).

[10] M. P. Harrison and R. M. Bradley, Phys. Rev. E **93**, 040802(R) (2016).

[11] R. Cuerno and A.-L. Barabási, Phys. Rev. Lett. **74**, 4746 (1995).

[12] M. Rost and J. Krug, Phys. Rev. Lett. **75**, 3894 (1995).

[13] R. Cuerno, M. Castro, J. Muñoz-García, R. Gago, and L. Vázquez, Nucl. Instrum. Methods Phys. Res., Sec. B **269**, 894 (2011).

[14] R. M. Bradley and J. M. E. Harper, J. Vac. Sci. Technol. A **6**, 2390 (1988).

[15] M. Kardar, G. Parisi, and Y.-C. Zhang, Phys. Rev. Lett. **56**, 889 (1986).

[16] M. Castro, R. Cuerno, L. Vázquez, and R. Gago, Phys. Rev. Lett. **94**, 016102 (2005).

[17] J. Muñoz-García, R. Gago, L. Vázquez, J. A. Sánchez-García, and R. Cuerno, Phys. Rev. Lett. **104**, 026101 (2010).

[18] M. Engler, S. Macko, F. Frost, and T. Michely, Phys. Rev. B **89**, 245412 (2014).

[19] J. Travis and J. Kring, *LabVIEW for Everyone: Graphical Programming Made Easy and Fun* (Prentice Hall, New Jersey, 2007).

[20] M. Castro, R. Gago, L. Vázquez, J. Muñoz-García, and R. Cuerno, Phys. Rev. B **86**, 214107 (2012).

[21] Y. Zhao, G.-C. Wang, and T.-M. Lu, *Characterization of Amorphous and Crystalline Rough Surface: Principles and Applications* (Academic Press, San Diego, 2001).

[22] S. Habenicht, W. Bolse, K. P. Lieb, K. Reimann, and U. Geyer, Phys. Rev. B **60**, R2200 (1999).

[23] J.-H. Kim, J.-S. Kim, J. Muñoz-García, and R. Cuerno, Phys. Rev. B **87**, 085438 (2013).

[24] J. F. Ziegler, M. D. Ziegler, and J. P. Biersack, Nucl. Instrum. Methods Phys. Res., Sect. B **268**, 1818 (2010).

[25] T. C. Kim, C.-M. Ghim, H. J. Kim, D. H. Kim, D. Y. Noh, N. D. Kim, J. W. Chung, J. S. Yang, Y. J. Chang, T. W. Noh, B. Kahng, and J.-S. Kim, Phys. Rev. Lett. **94**, 139602 (2005).

[26] J-H. Kim, N.-B. Ha, J.-S. Kim, M. Joe, K.-R. Lee, and R. Cuerno, Nanotechnol. **22**, 285301 (2011).

[27] J. Muñoz-García, M. Castro, and R. Cuerno, Phys. Rev. Lett. **96**, 086101 (2006).

[28] J. Muñoz-García, R. Cuerno, and M. Castro, Phys. Rev. B **78**, 205408 (2008).

[29] J. Renedo, R. Cuerno, M. Castro, and J. Muñoz-García, Phys. Rev. B **93**, 155424 (2016).

[30] A. Moreno-Barrado, M. Castro, R. Gago, L. Vázquez, J. Muñoz-García, A. Redondo-Cubero, B. Galiana, C. Ballesteros, and R. Cuerno, Phys. Rev. B **91**, 155303 (2015).

[31] J. Muñoz-García, R. Cuerno, and M. Castro, Phys. Rev. B **100**, 205421 (2019).

[32] M. Castro and R. Cuerno, Phys. Rev. Lett. **94**, 139601 (2005).

[33] H. Hofsäss, O. Bobes, and K. Zhang, J. Appl. Phys. **119**, 035302 (2016).

[34] J. Muñoz-García, R. Cuerno, and M. Castro, Phys. Rev. E **74**, 050103(R) (2006).

[35] O. Bobes, K. Zhang, and H. Hofsäss, Phys. Rev. B **86**, 235414 (2012).

[36] H. Gnaser, *Low Energy Ion Irradiation of Solid Surfaces* (Springer-Verlag, Heidelberg, 1999).

[37] A. Moreno-Barrado, R. Gago, A. Redondo-Cubero, L. Vázquez, J. Muñoz-García, R. Cuerno, and M. Castro, Europhys. Lett. **109**, 48003 (2015).

[38] G. Carter, Appl. Phys. Lett. **71**, 3066 (1997).

[39] M. Raible, S. J. Linz, and P. Hänggi, Phys. Rev. E **64**, 031506 (2001).

[40] J. Muñoz-García, R. Cuerno, and M. Castro, J. Phys.: Condens. Matter **21**, 224020 (2009).

[41] D. A. Pearson and R. M. Bradley, J. Phys.: Cond. Matter **27**, 015010 (2015).

[42] M. P. Harrison, D. A. Pearson, and R. M. Bradley, Phys. Rev. E **96**, 032804 (2017).

[43] A. Keller, S. Roßbach, S. Facsko, and M. Möller, Nanotechnol. **19**, 135303 (2008).

[44] A. Keller, R. Cuerno, S. Facsko, and W. Möller, Phys. Rev. B **79**, 115437 (2009).

[45] K. M. Loew and R. M. Bradley, Phys. Rev. E **100**, 012801 (2019).

[46] R. M. Bradley (private communication).